Geophys. J. Int. (2007) **170,** 971–985 doi: 10.1111/j.1365-246X.2007.03457.x

GJI Geodesy, potential field and applied geophysics

Moho undulations beneath Tibet from GRACE-integrated gravity data

Young Hong Shin,[1] Houze Xu,[2] Carla Braitenberg,[3] Jian Fang[2] and Yong Wang[2]

[1] *Korea Astronomy and Space Science Institute, Yuseong-gu, Daejeon* 305-348*, Korea. E-mail: yhshin@kasi.re.kr*
[2] *Institute of Geodesy and Geophysics, Chinese Academy of Sciences,* 54 *Xudong Road,* 130077 *Wuhan, P. R. China*
[3] *Department of Earth Sciences, University of Trieste, Via Weiss* 1, 34100 *Trieste, Italy*

Accepted 2007 March 28. Received 2007 March 28; in original form 2006 February 17

SUMMARY

Knowledge of the variation of crustal thickness is essential in many applications, such as forward dynamic modelling, numerical heat flow calculations, seismologic applications and geohistory reconstructions. We present a 3-D model of the Moho undulations over the entire Tibetan plateau derived from gravity inversion. The gravity field has been obtained by using the Gravity Recovery and Climate Experiment (GRACE) potential field development which has been integrated with terrestrial data, and is presently the best available in the studied area. For the effective use of the global geopotential model that has no height information of observation stations, upward continuation is applied. The Moho model is characterized by a sequence of troughs and ridges with a semi-regular pattern, which could reflect the continent–continent collision between the Indian and Eurasian plates. The three deep Moho belts (troughs) and shallow Moho belts (ridges) between them are clearly found to have an E–W directional trend parallel to the border of the plateau and tectonic lines, while variation of the directionality is observed in central to southeast Tibet. To describe the distinctive shape of the Moho troughs beneath Tibet, we introduce the term, 'Moho ranges'. The most interesting aspects of the Moho ranges are (1) that they run in parallel with the border and tectonic sutures of the plateau, (2) that the distances between ranges are found at regular distances of about 330 km except in northeast Tibet and (3) that the splitting of the ranges into two branches is found as the distance between them is increasing. From our study, we conclude that the distinctive undulations of the Tibetan Moho have been formed by buckling in a compressional environment, superimposed on the regional increase in crustal thickness. According to our analysis, the GRACE satellite-only data turns out to have good enough resolution for being used to determine the very deep Moho beneath Tibet. Our Moho model is the first one that covers the entire plateau.

Key words: GRACE, gravity inversion, Moho buckling, Moho ranges, Tibet, upward continuation.

1 INTRODUCTION

Since the satellite gravity data from CHAMP (launch on 2000 July 15) and Gravity Recovery and Climate Experiment (GRACE, 2002 March 17) were released to the public, great attention has been paid to the recovery of high resolution gravity and its temporal variation from Earth-observing satellites. Further improvement of the global gravity field with higher resolution will be obtained with the satellite program GOCE, to be launched in 2007 (refer to http://www.gfz-potsdam.de/, http://www.csr.utexas.edu/ and http://www.esa.int/esaLP/ESA1MK1VMOC_LPgoce_0.html). The major benefit of the gravity recovery from satellites is its ability to provide precise and uniform gravity data with global data coverage and the temporal variation of the field. Though the satellite-based gravity data have been thought to be unsuitable for Moho estimation due to their poor resolution, we show that the most recent model from the GRACE mission can give us a Moho image in Tibet, where the Moho lies very deep and the extent of terrestrial gravity data is relatively poor.

This work aims at determining the 3-D Moho structure model beneath Tibet by using the satellite data according to the most recent GRACE Gravity Model (GGM). We analyse the gravity field critically, and discuss in which areas there is lack of terrestrial data, which explains the large discrepancies found locally between the older EGM96 and the new GRACE gravity field harmonic expansion. Thus, to improve the satellite-based analysis we propose a no-terrestrial-gravity-data zone (NGZ) correction for the area where no terrestrial gravity data are available, in addition to the upward continuation to a level higher than topography. The Moho model is the result of a

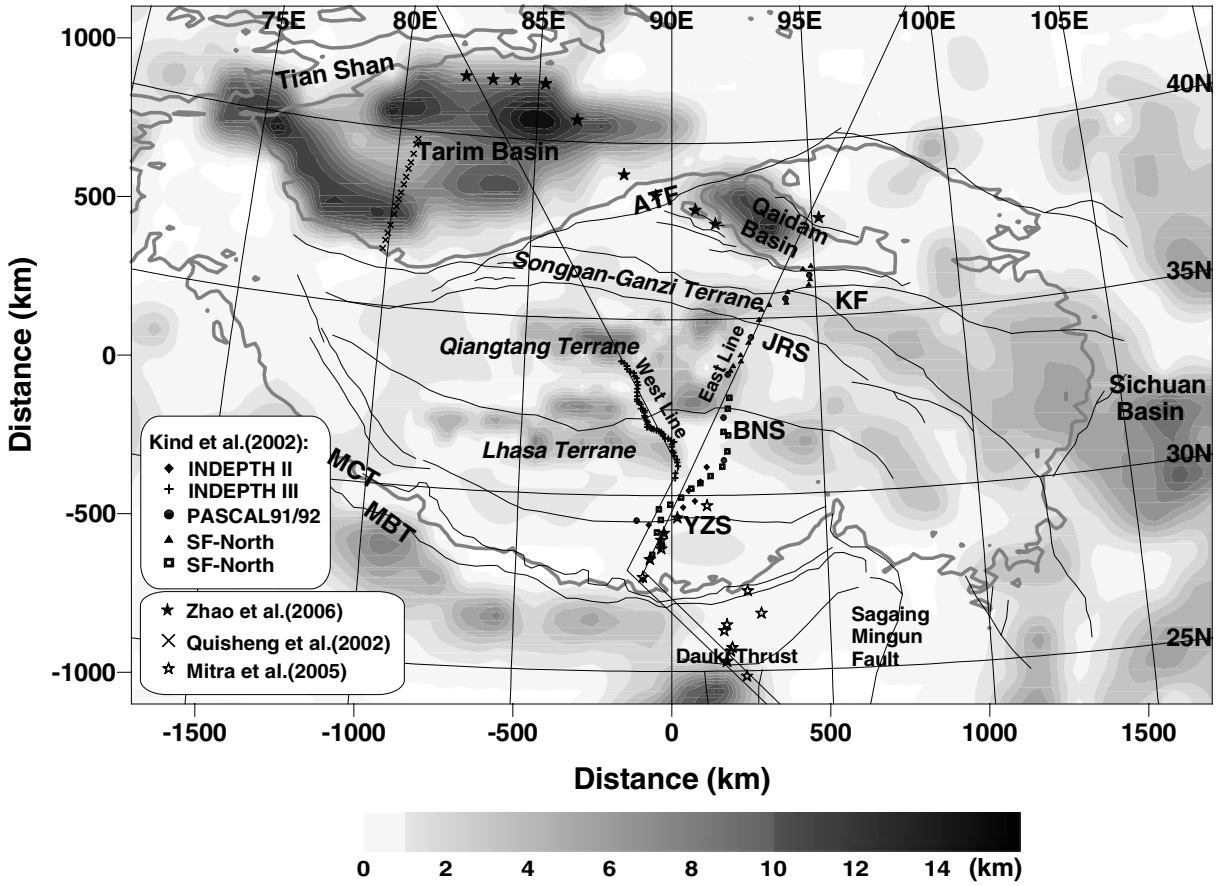

Figure 1. Sediment thickness model from Institute of Geodesy and Geophysics (IGG, Chinese Academy of Science) and station locations of seismic experiments. Profiles along east and west lines are given in Fig. 13.

constrained gravity inversion, which includes the correction for the sediment thickness. The crustal thickness variations over the Tibetan plateau have been determined along seismic profiles during several international campaigns (e.g. INDEPTH, PASSCAL; http://www.geo.cornell.edu/geology/indepth/indepth.html, http://www.iris.edu/about/PASSCAL/, http://www.gfz-potsdam.de/pb2/pb24/projects/indepth/twolines/twolines.html) and cover mostly the central part of Tibet, whereas the eastern and western parts are poorly covered. The location of the published seismic transects are shown in Fig. 1. It is evident that the seismic lines do not cover large portions of the plateau and, therefore, that large uncertainties on the crustal thickness variations exist.

The Tibetan Plateau formed by large-scale continental collision and continuous convergence between the Indian and Eurasian plates, which began about 50 ± 10 Ma (e.g. Zhou *et al*. 1998). The plateau consists of several tectonic terranes, the Kunlun, Qiangtang, Lhasa and Himalayan, separated by three sutures, the Bangong-Nujiang (BNS), Jinsha River (JRS) and Yarlung-Zangbo (YZS). The first three tectonic blocks are believed to have been accreted successively to southern Asia before the collision as the deformation becomes younger southwards across the plateau. The YZS now marks the location of the last oceanic subduction before the continental collision (e.g. Zhou *et al*. 1998). It is therefore, an interesting question, whether the crustal thickness variations reflect the directionalities imposed by the presence of the terranes, or whether it is independent and is rather influenced by the NS-trending rifts present in central Tibet. The passive and active seismic investigations across the plateau, as for example, those of the INDEPTH and the earlier campaigns, can partly give an answer, as they obliquely cross the different terranes. It has been found that the crustal thickness indeed varies across the terrane, imposing a modulation on the 70 km depth range typical of the Tibet plateau.

The recent work of Kind *et al*. (2002) combined all available high-quality teleseismic earthquake records and used the receiver function technique along the two cross-sections shown in Fig. 1. They find that the maximum thickness occurs within the Lhasa terrane about 100 km north of the Yarlung-Zangbo suture (about 30°N). Immediately to the north, the Moho shallows to its minimum depth and then maintains a roughly constant depth to the northern margin of the plateau (within a few km). Qualitatively similar results were found by Mitra *et al*. (2005), with the difference that for the same stations used by Kind *et al*. (2002), a 10 km deeper Moho is found, and the northwards deepening is more accentuated. There is some controversy on the presence of Moho steps in correspondence to the sutures, dividing the authors that claim to have detected Moho steps at the YZS and the BNS from those that report a continuous Moho (e.g. Kind *et al*. 2002, Mitra *et al*. 2005). The study of the northwest Tibet and its transition to the Tarim basin gave evidence of a southward-dipping of the Moho in the southern Tarim basin (Quisheng *et al*. 2002), with increasing Moho depths below the Kun Lun. Further east, the transition from Tarim across the Altyn Tagh range into the Qaidam basin (Zhao *et al*. 2006) gave evidence of a shallowing of the Moho towards both basins (see Fig. 1). We intend to verify whether these Moho undulations can be extended east and west of the seismic profiles, and whether the Moho undulations can be correlated to the presence of the different terranes (see Fig. 1).

Ideally, it would be interesting to make a full 3-D-density structure of the entire area, in order to model the new gravity data. This is impossible due to the lack of seismic constraints and the lack of knowledge on the density variations. Therefore, the complexity of the model must be reduced. The greatest density jump in the lithosphere is at the Moho, followed by the density reduction due to sediments. The effect of lithospheric thickening is much smaller, as the density contrast of the lithosphere to the asthenosphere is less than one tenth the value at the Moho and the depth of the lithosphere–asthenosphere transition is much lower (PREM, Preliminary Earth Reference Model). When reducing complexity, it is thus justified to consider the two units that will primarily contribute to the gravity signal, which are the Moho and the sediment-package. The sediments can be modelled directly, as in the studied area a sediment thickness model is available that has been obtained from a combination of shallow seismics and geological mapping by the Chinese authorities (Lithospheric Dynamic Atlas of China 1989). The residual gravity field can be used for inverting for the Moho undulations. The inversion method (see chapter 3) can accept lateral density variations, if such information is available. In the case such information is lacking, a constant density is the only viable method. It should be though considered, that a local density reduction leads to a local increase of the Moho undulation amplitude with respect to the reference depth. The amplitude increase is in a linear relation to the density contrast reduction. In the case that a layered structure is assumed, as shown, for example, by Blakeley (1995), the different contributions can be separated by frequency filtering, making use of the general property of the gravity field, that the amplitudes of the signals are reduced by a near to exponential factor with depth: therefore, the higher frequencies pertain to shallower sources, and can be eliminated by a high pass filtering of the gravity data prior inversion.

The Moho undulations in Tibet area were first determined by a constrained inversion of the gravity field derived from purely terrestrial data by Braitenberg *et al*. (2000a,b). In a second step the plateau and Tarim basin were characterized in terms of flexural rigidity, or equivalently, effective elastic thickness (Jin *et al*. 1996; Braitenberg *et al*. 2003). An isostatic flexure study of the eastern margin of Tibet and the transition to the Sichuan basin was made by Jiang & Jin (2005).

In this research, we present an updated model of the Moho undulations on an extended area and using an improved gravity data set, which at long wavelengths relies entirely on the new results of the GRACE-satellite mission. The gravity data set is the best presently available for estimating the Moho of the Tibetan plateau and surrounding areas.

2 DATA

The GGM02C is the principle gravity data set used in our study. The EGM96 (higher orders than 200) and Topographic/Isostatic gravity model (TIGM) are used to supplement the analysis. We also use a data set of 30 arcmin × 30 arcmin sedimentary thickness information (Fig. 1) provided by the Institute of Geodesy and Geophysics (IGG, Chinese Academy of Science), which is based on a collection of different data, mainly seismic investigations (Lithospheric Dynamic Atlas of China 1989). For the Tarim basin details on the sediment sequence can be found in Chen & Shi (2003) and in Sobel *et al*. (2003). The JGP95E 5′ that was developed to support the EGM96 (Lemoine *et al*. 1998) is adopted as our topographic data.

2.1 GGM02C

The GGM02C model from the GRACE mission has been obtained from the combination of the satellite derived gravity field and terrestrial gravity data. In the harmonic expansion, the coefficients up to degree and order 120 are purely from the satellite measurements, the degrees 120 to 200 have been obtained by a combination of the purely satellite gravity data and the terrestrial data, in the form distilled in the EGM96 harmonic expansion (Tapley *et al*. 2005). The combined field, from order up to 200 is freely available from the GRACE homepage (http://www.csr.utexas.edu/grace/gravity/) and is termed GGM02C. Details on the construction of the field are found in Tapley *et al*. (2005).

In general, the improvement of lower harmonics of the GGM02C with respect to the EGM96 model is very important not only in geoid computation but also in Moho estimation, since the low harmonics are closely related with deep subsurface structures like the Moho and the deeper interior of the Earth. The improvement of the gravity recovery of the GGM02C is shown in Fig. 2, of which the accumulated error at degree 120 is estimated to be only about 1.5 MGal, significantly better than the value of about 4.9 MGal of EGM96. The improvement with respect to the EGM96 model is particularly evident for the Tibet area, where due to high altitude and inaccessibility vast areas with no terrestrial gravity measurements (no-terrestrial-gravity-data zones, NGZ) exist (Fig. 3), which cover the western part and the southern border of the plateau. The data quality and areas with missing data are shown in Fig. 3, and it is evident that due to the large lateral extent the influence on the spherical harmonic expansion is to be expected also on low harmonic coefficients. The low accuracy of 19 MGal of the terrestrial gravity data set, used for EGM96 in most of the plateau, is due to sparseness of data and to the influence of the mountainous terrain of the Himalayas (Lemoine *et al*. 1998). Fig. 4 shows the difference between the two models (GGM02C and EGM96) up to degree and order 120. The differences are over 20 MGal and reach up to about 80 MGal, demonstrating the important achievement of the satellite mission. The root mean square difference in this area between GGM02C and EGM96 for the development up to degree and order 120 (200) is 14 (15) MGal, the differences between the extremal values being −69 and +77 MGal (−69 and +84 MGal).

After completion of the manuscript, a further public spherical harmonic expansion EIGEN-GL04C of the GRACE, LAGEOS and terrestrial derived gravity field was published, which is complete to degree and order 360 (Förste *et al*. 2006). At the time of writing, the details on the terrestrial data used in the Himalaya–Tibet area were not available, so the NGZ is unknown. A comparative discussion is made below, in the frame of the NGZ correction.

2.2 EGM96 and TIGM

The EGM96 is also a widely used global geopotential model, of which low ($n \leq 70$) and high degrees were determined from several decades of satellite tracking and surface gravity of various sources, respectively. The EGM96, when it was made by NASA Goddard Space Flight Center(NASA GSFC) and National Imagery and Mapping Agency (NIMA), was designed to include terrestrial gravity data over China that had not been available before (Lemoine *et al*. 1998). Due to the limited maximum degree of the EGM96, our analysis hardly resolve full wavelength of 93 km nor better at middle latitude of our study area.

During the development of EGM96, TIGM spherical harmonic potential coefficients were also derived based on the digital terrain

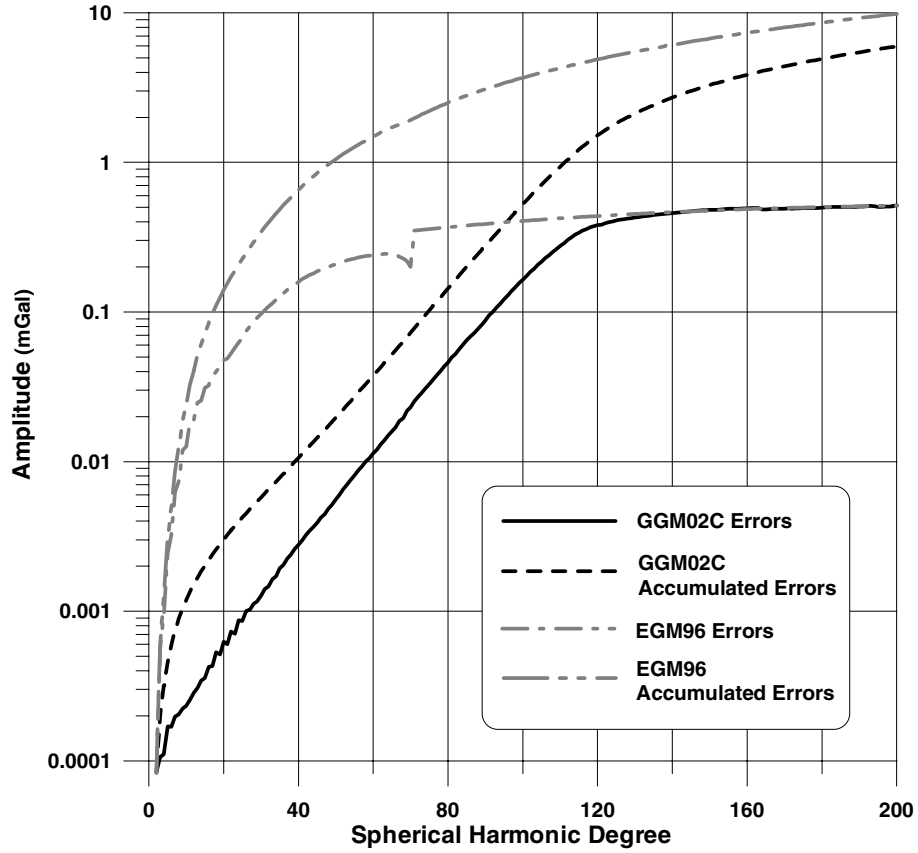

Figure 2. Amplitude of gravity errors of the GGM02C and the EGM96; computed from the standard deviation coefficients of the models.

model, JGP95E for the area where no gravity data were available (Lemoine *et al*. 1998). While the coefficients from degree 2 to 40 are exactly those of the satellite-only solution EGM96S, the coefficients from degree 41 to 360 are obtained from an expansion of the topographic/isostatic potential implied by the Airy/Heiskanen hypothesis with constant depth of compensation 30 km. It follows that in the combination of the GGM02C and EGM96 solution, in the no gravity data zone, the gravity field is affected by the Airy/Heiskanen isostatic assumption. This fact will be taken into account in the step of upward-continuing the data to the level above maximum topography.

3 METHODOLOGY

3.1 Upward continuation

We have applied the upward continuation in order to propagate the known field at ellipsoidal level to a level that lies above the topography. For a thorough mathematical treatment in potential theory we refer to standard texts (e.g. Heiskanen & Moritz 1987; Blakely 1995) and a report focused on the topic by Cruz & Laskowski (1984). If spherical harmonic coefficients are selected for upward continuation, the process is very simple and the truncation error due to the limit of the integration range can be easily overcome, while the truncation above maximum degree is still unavoidable due to the limit of maximum degree of the potential model. The gravity anomaly at the height H above the reference ellipsoid can be computed by substituting the value r by $a+H$ in eq. (1) (Cruz & Laskowski 1984):

$$\Delta g(r,\overline{\phi},\lambda) = \frac{GM}{a^2}\sum_{n=2}^{\infty}(n-1)\left(\frac{a}{r}\right)^{n+2} \times \sum_{m=0}^{n}(\overline{C}^{*}_{nm}\cos m\lambda + \overline{S}_{nm}\sin m\lambda)\overline{P}_{nm}(\sin\overline{\phi}) \quad (1)$$

a	Equatorial radius
GM	Geocentric gravitational constant
$\overline{C}^{*}_{nm}$, $\overline{S}_{nm}$	Fully normalized spherical potential coefficients $*$ means even-degree zonal reference values subtracted
$\overline{P}_{nm}$	Fully normalized Legendre functions
r, $\overline{\phi}$, λ	Geocentric radius, latitude, longitude

The upward continuation via Poisson's integral formula (Heiskanen & Moritz 1987) in spherical coordinates is given by eq. (2):

$$V_e(r,\theta,\lambda) = \frac{R(r^2-R^2)}{4\pi}\int_{\lambda'=0}^{2\pi}\int_{\theta'=0}^{\pi}\frac{V(R,\theta',\lambda')}{l^3}\sin\theta' d\theta' d\lambda', \quad (2)$$

$$l = \sqrt{r^2+R^2-2Rr\cos\psi}$$

$$\cos\psi = \cos\theta\cos\theta' + \sin\theta\sin\theta'\cos(\lambda'-\lambda)$$

V_e	Potential at a exterior point $(r,\theta,\lambda)$of a sphere
V	Potential at a point (R,θ,λ)on a sphere

The plane approximation or Fourier domain expression can be found in the texts listed above.

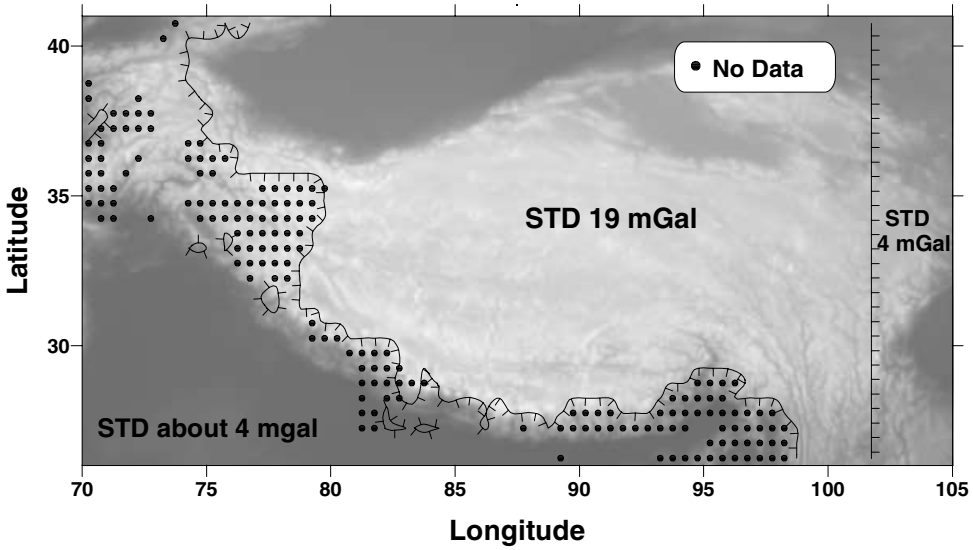

Figure 3. Terrestrial gravity data quality in Tibet: Black solid circles show places where no 30 arcmin × 30 arcmin terrestrial gravity data were used for EGM96. Background image represents topography.

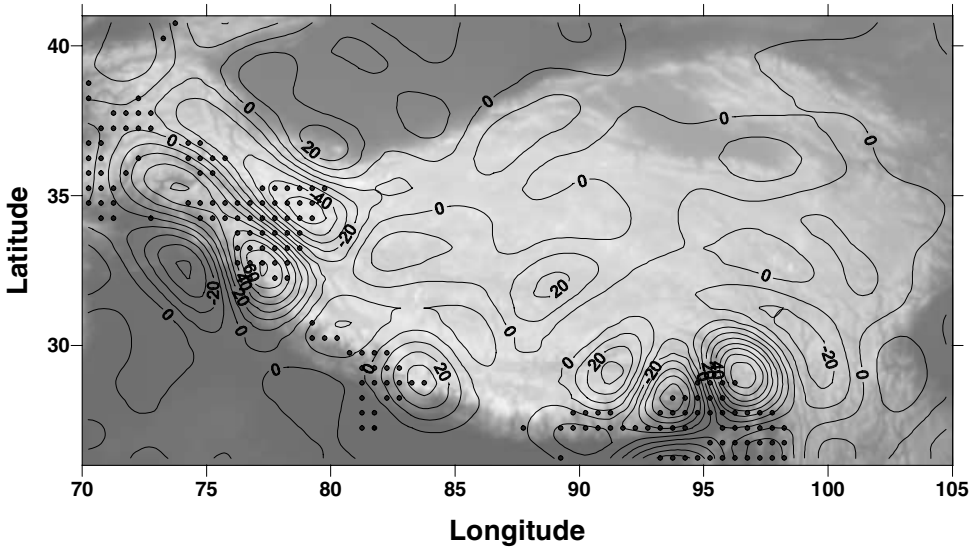

Figure 4. Gravity anomaly difference between GGM02C and EGM96: maximum degree and order 120. Black solid circles show places where no 30 arcmin × 30 arcmin terrestrial gravity data were used for EGM96. Background image represents topography. Contour interval 20 MGals.

3.2 Gravity effect of terrain and sediments

The gravity effect on a point $P(r, \theta, \lambda)$ caused by a mass element $dM(r', \theta', \lambda')$ in a spherical coordinates can be derived as

$$d\overrightarrow{g} = \left(\frac{r - r'\cos\psi}{l^3}\right) G dM, \tag{3}$$

where G the Newton's gravitational constant, $dM = \rho r'^2 \sin\theta'\, dr'\, d\theta'\, d\lambda'$, ρ density and ψ angular distance same as in eq. (2). The gravity effect of topography and sediment can be estimated by integrating the gravity of each mass element.

3.3 Use of Fourier transform in gravity inversion

The next eq. (4) derived by Parker (1972) shows the relation between the vertical gravity effect, Δg and its causative mass topography, $h(\vec{r})$ in wavenumber domain.

$$F[\Delta g] = -2\pi G\rho \exp(-|\vec{k}|z_0) \sum_{n=1}^{\infty} \frac{|\vec{k}|^{n-1}}{n!} F[h^n(\vec{r})], \tag{4}$$

where $\vec{r}$ denotes the projection of the position $r = (x, y, z)$ onto the $x - y$ plane, $\vec{k}$ the wave vector of the transformed function, G the Newton's gravitational constant, ρ the density and $F[]$ is the Fourier transform. eq. (4) is convergent in the whole k-plane, when $\max|h(\vec{r})| < z_0$ and $z_0 > 0$ (Parker 1972). Hence eq. (4) provides an easy and timesaving way to compute the gravity effect caused by a subsurface mass anomaly or topography. Oldenburg deduced an algorithm (Oldenburg 1974), so called Parker–Oldenburg method, to compute the topography of a density discontinuity surface from the gravity anomaly by inversion of eq. (4). It is modified here for

the 3-D case (eq. (5)) and applied to compute the Moho structure.

$$F[h(\vec{r})] = -F[\Delta g(\vec{r})]\exp(|k|z_0)/(2\pi G\rho) - \sum_{n=2}^{\infty}\frac{|\vec{k}|^{n-1}}{n!}F[h^n(\vec{r})]. \quad (5)$$

The method is an iterative inversion scheme, which alternates the inverse (eq. 5) and forward calculation (eq. 4) repeatedly. In the first step $h(\vec{r}) = z_0$. The final result depends on the choice of the reference depth z_0 and the density. A greater reference depth increases the amplitude of the Moho oscillation; an increase of the density reduces the amplitude of the Moho undulation, in an inverse linear relationship.

To monitor the convergence of the forward algorithm in eq. (5), the criterion defined in eq. (6) is used.

$$S_n = \max_{\substack{\text{overall}\\ k}}\left|\frac{|k|^{n-1}}{n!}F[h^n(\vec{r})]\right|. \quad (6)$$

The summation of the right term in eq. (5) is done until $S_n/S_2 < E$ is satisfied, where E is a sufficiently small number. The high frequency waves are suppressed by using a low-pass filter defined as follows:

$$B(k) = \left[\frac{1}{2}\left\{1+\cos\left(\frac{\pi(k-w_1)}{w_2-w_1}\right)\right\}\right]^{kp} \qquad \begin{matrix}1 & |k|\langle w_1\\ w_1 \le |k| \le w_2\,, & (7)\\ 0 & |k|\rangle w_2\end{matrix}$$

where kp is a positive integer and w_1 and w_2 are wavenumber parameters. Longer waves ($|k| < w_1$) pass through the filter, but shorter waves ($|k| > w_2$) are cut off, while intermediate waves pass in parts. The value of kp defines the steepness of the filter function. Two FORTRAN programs by Shin *et al*. (2006) were used.

3.4 Coherence

The coherency, γ and coherence, γ^2 are given by

$$\gamma = \frac{C}{E_0^{1/2}E_1^{1/2}}, \quad (8)$$

and

$$\gamma^2 = \frac{C^2}{E_0E_1}, \quad (9)$$

where

$$\begin{aligned} E_0 &= \langle H\cdot H^*\rangle\\ E_1 &= \langle B\cdot B^*\rangle\\ &= \langle W\cdot W^*\rangle\,(2\pi\Delta\rho G)^2e^{-2kz},\\ C &= \langle H\cdot B^*\rangle\\ &= \langle H\cdot W^*\rangle\,(2\pi\Delta\rho G)e^{-kz}\end{aligned}$$

where H, B and W represent topography, Bouguer anomaly (BA) and Moho undulation, respectively (Forsyth 1985; Jin *et al*. 1994). And '$<\ >$' denotes average over narrow wavenumber bands and '$*$' complex conjugation. The coherence is the squared value of the coherency, which keeps track of the fact whether the two quantities are correlated or in anticorrelation.

eq. (9) reduces to

$$\gamma^2 = \frac{\langle H_TW_T + H_BW_B\rangle^2}{\langle H_T^2+H_B^2\rangle\langle W_T^2+W_B^2\rangle}, \quad (10)$$

if surface loading and subsurface loading are statistically independent. Subscripts T and B represent loads on top and bottom, respectively (Forsyth 1985). The f-ratio, the ratio of bottom to top loading, is given as a function of wavenumber with formula,

$$f = \Delta\rho W_{\text{Initial}}/\rho_0H_{\text{Initial}}, \quad (11)$$

where subscript '*Initial*' means initial loading (Forsyth 1985).

4 THE GRAVITY FIELD AND ITS REDUCTIONS

4.1 Gravity anomalies on a defined height level

The reference level of the gravity anomaly is set to 7 km above mean sea level (MSL), which is a little higher than maximum topography (the highest level is 6.71 km based on the JGP95E) in order to reduce the error of shallow layers that is usually caused by under or overestimation of terrain and sediment effects. Though this upward continuation has been rarely used in gravity inversion modelling, it is quite useful in data processing of satellite gravity that has no height information of observation stations. The loss of short-wave signals that might occur during the upward continuation is negligible as long as the reference level is set to be just a little higher than the topography. Though the upward continuation technique can be applied for smoothing or filtering of gravity field, our purpose here shouldn't be considered to be equivalent with that. The free-air anomaly (FA) at the reference level is easily computed from the GGM02C (up to degree 200) and the EGM96 (degree 201–360) by using eq. (1). The values are contained between a minimum of −203 and a maximum of 235 MGal, with a mean of −9 MGal and a standard deviation (*SD*) of 42 MGal (in domain: 55°E–120°E and 15°N–50°N). The BA is computed with eq. (3) by eliminating the gravity effect of the terrain above MSL and by filling up the mass deficiency in oceans and sedimentary basins via eq. (3) in spherical coordinates. For computing the terrain effect we used the values $dr = 1$ km, $d\lambda$ and $d\theta = 0.5$ arcmin for integration of inner zone within $4^\circ \times 4^\circ$, while $dr =$ not divided, $d\lambda$ and $d\theta = 5$ arcmin for the outer zone; Double size of $d\lambda$ and $d\theta$ were used for computing the sediment effect; The integrating radius is set to be 5° in angular distance and the densities are set to 2670 kg m^{-3}, 1030 kg m^{-3} and 2030 kg m^{-3} for continent, ocean and density difference of sediment, respectively. We performed the computation over a wide area, 55°E–120°E and 15°N–50°N that includes the study area and its neighbouring regions. The sediment correction reaches the maximum value of 116 MGal, in agreement with that found in Braitenberg *et al*. (2003). The terrain contributes to a correction up to a maximum of 634 MGal. The final corrected BA has values between −596 and 153 MGal, with mean −124 MGal and *SD* 153 MGal.

4.2 NGZ correction and its upward continuation

We also introduced the NGZ correction for the reduction of the big errors that were observed in the region where no terrestrial gravity data were available, especially near the southern border of the study region (see big anomalous highs and lows and bull's-eye patterns uncorrelated with topography in Fig. 5A). As mentioned above, in developing the EGM96 model the TIGM was used to fill up the gap of the NGZ, where satellite gravity data only up to 40° were used. The NGZ correction must be made due to the fact that the TIGM in EGM96 has been made for degrees 41–360; Now we have better satellite gravity data from the GRACE mission: according to the reliability analysis of the satellite-only data (Tapley *et al*. 2005), we use the GGM02C only up to degree 120 and the TIGM from degree 121 to 360 for the NGZ. The substitution of data with the TIGM in the NGZ introduces some errors that are spread over a

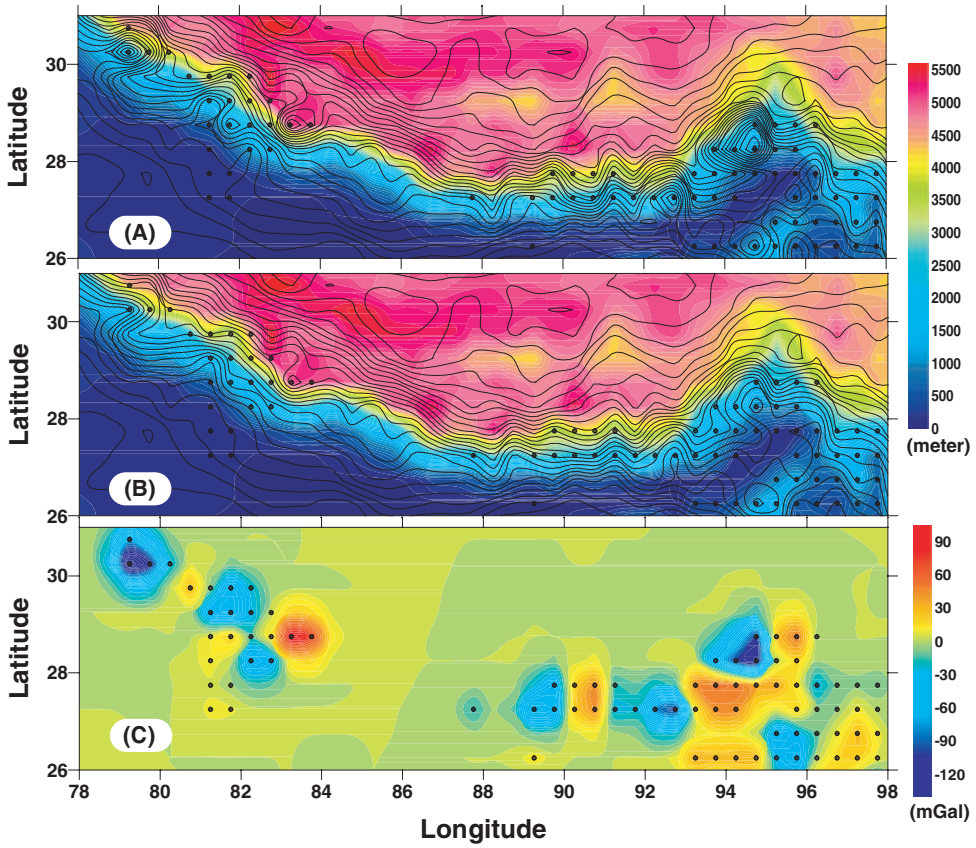

Figure 5. Bouguer anomaly (BA) and no-terrestrial-gravity-data zone (NGZ) correction near south border: (A) BA before NGZ correction, (B) BA after NGZ correction, (C) NGZ correction. Black solid dots: NGZ. Background colour scale in (A) and (B): Topography. Solid line: Bouguer anomaly in 20 MGal interval. Colour scale in (C) represents NGZ correction. Reference level: 7 km above MSL.

large window of degrees, up to 360, and must be corrected. The point of NGZ correction is that the new satellite-based gravity data (up to degree 120) replaces the old model (up to degree 40) at NGZ and that the TIGM is used only for higher degrees (121–360). This correction process is performed by calculating the difference between the TIGM field and the gravity expansion and then by applying an upward continuation, as explained below.

The difference between TIGM (degrees 121–360) and GGM02C (121–200)/EGM96 (201–360) varies from −168.3 to 119.2 MGal in the NGZ defined by 55°E–120°E and 15°N–50°N. This implies that the poor resolution of the satellite gravity for EGM96 still influences the high degrees (121–360) of GGM02C/EGM96. We use the above-defined difference for the NGZ correction on MSL: V^C. As mentioned above our reference level is set to 7 km-height above MSL It should thus be noted that errors of NGZ could propagate to neighbouring areas during the upward continuation via eq. (1) if the FA on the reference level is computed directly from the GGM02C/EGM96 that already includes the TIGM. In order to minimize the error propagation, we followed the following procedures based on the linearity: With $V = V^0 + V^C$, the eq. (2) allows V_e to be divided into $V_e^0 + V_e^C$, where V_e^0 and V_e^C are potentials at exterior points from V^0 and V^C, respectively. Suppose that V^0 is the FA from GGM02C/EGM96 and V^C the NGZ correction term on MSL. Then V_e^0 and V_e^C would be their upward continuations up to the reference level. Hence V_e^0 can be computed more easily from eq. (1) than eq. (2), and V_e^C, the NGZ correction term from eq. (2) or other upward continuation methods. Its correction value on the reference level varies from −133.2 to 91.2 MGal (the correction results of this section represent 30 × 30 min averages from the grid size of 10-arcmin. Integration is performed over an area with radius 3-arcdegrees, and grid sizes are again divided into 1-arcmin for the inner zone of 4° × 4°). Fig. 5(B) shows that the big errors in Fig. 5(A) were considerably reduced through the NGZ correction. The large NGZ correction is restricted to some parts of the study area, especially at the southern border (Fig. 5C). While the area close to the NGZ is largely affected by the error propagation, the effect decreases rapidly with the distance.

We have compared the gravity field of the GGM02C (up to 200)/EGM96 (201–360) expansion with that of EIGEN-GL04C for degree and order up to 120 and 360, respectively. The difference up to degree 120 shows small variation of −7.9 to 6.5 MGal with average and *SD* 0.017 ± 2.042 MGal (Fig. 6A), while the one of up to degree 360 shows great variation of −124.9 to 179.7 MGal with average and *SD* 0.011 ± 30.74 MGal (Fig. 6B). The greatest differences are found in the NGZ, and show good correlation with the NGZ-correction. The maximum difference-values are greater than the NGZ-correction, due to interpolation and averaging of the latter.

4.3 BA overview

The BA we use for the gravity inversion is shown in Fig. 7. Thanks to the GRACE mission, the problem of data coverage of the entire plateau is well overcome. An E–W directional trend prevails in the plateau. Rapid variation of the BA is observed along the border of the plateau, and the most negative BA is observed at the region 200–300 km inside the plateau-border, while it varies smoothly in

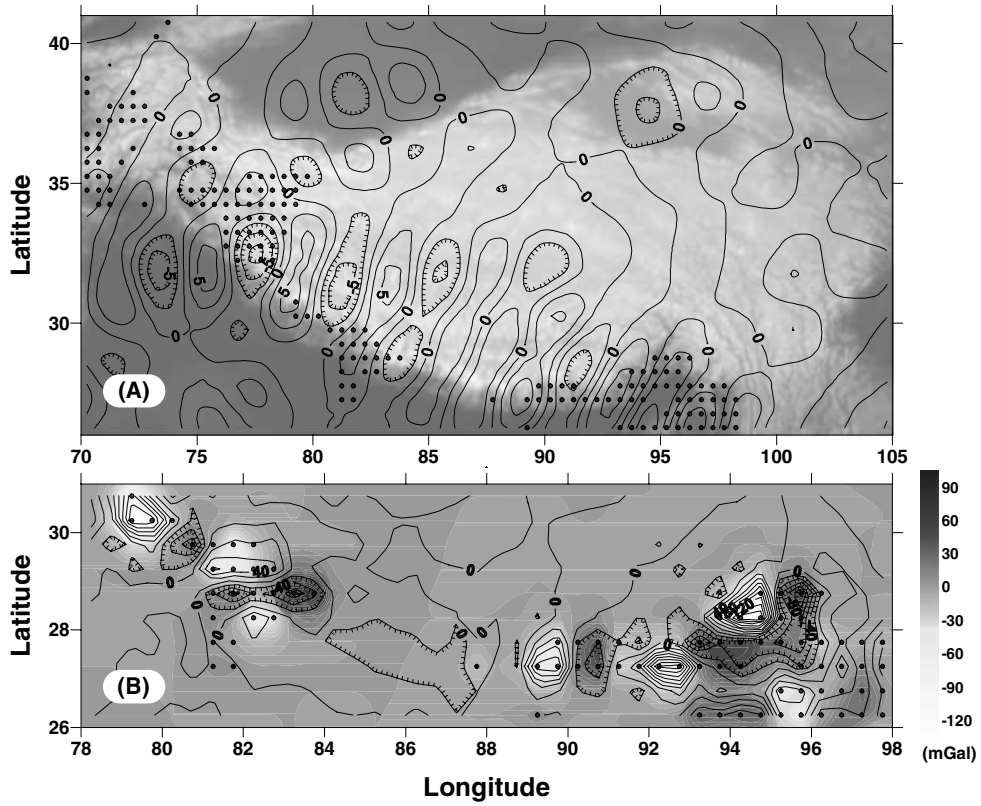

Figure 6. Comparison with EIGEN-GL04C model: (A) gravity difference between GGM02C and EIGEN-GL04C (up to 120) and (B) NGZ correction and gravity difference between GGM02C/EGM96 and EIGEN-GL04C (up to 360). Background grey scale and contours in (A) represent topography and gravity difference in 2.5 MGal interval, respectively. It varies −7.9 to 6.5 MGal with average and standard deviation (*SD*) 0.017 ± 2.042 MGal. Grey scale in (B) represents NGZ correction and contours gravity difference in 20 MGal interval. NGZ correction ranges −133.2 to 91.2 with average and *SD* −2.15 ± 20.38 MGal, while the gravity difference −124.9 to 179.7 and 0.011 ± 30.74 MGal, respectively. Black solid circle: NGZ. Reference level: 7 km above MSL.

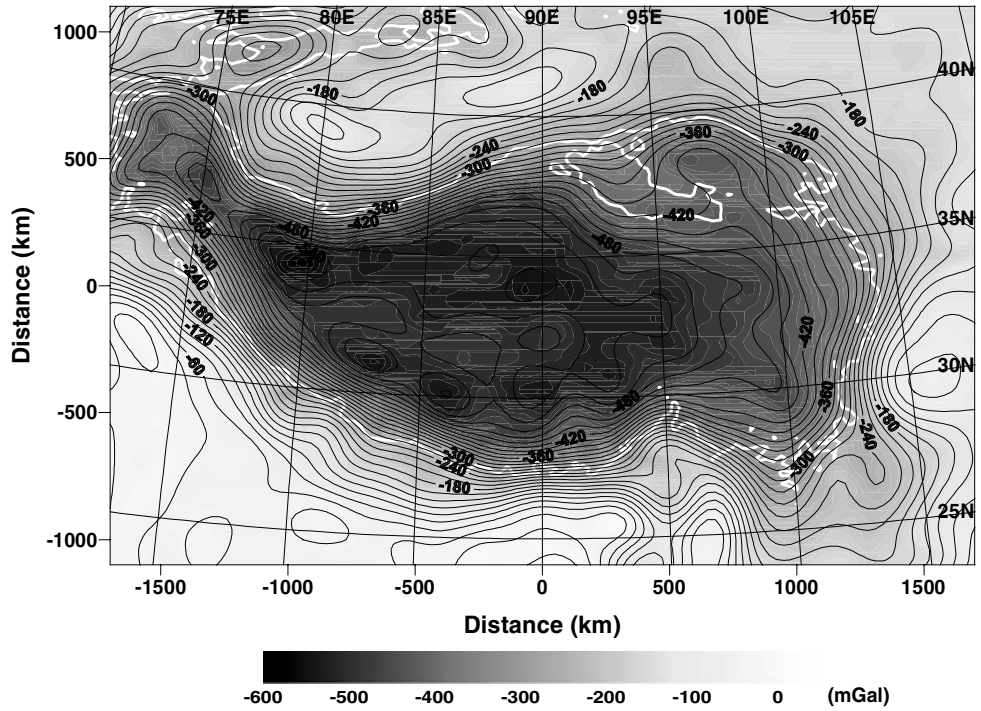

Figure 7. Bouguer anomaly (BA): BA was represented in grey scale and the low-pass filtered BA in contour lines in 20 MGal interval. The plateau is outlined with white line, contour of 3 km-height level. All waves longer than 310 km were passed through the filter, waves shorter than 220 km were filtered out, and waves between them were reduced in amplitude. Refer to the text for details of filter design.

the central part of the plateau. The trends become weak in the eastern Tibet. The Tarim basin has values between −100 and −180 MGal, the more negative values being found towards the borders of the basin.

5 GRAVITY INVERSE MODEL

The gravity field contains important signals due to mass anomalies in the subsurface, so that reasonable and useful information can be obtained from the gravity inversion with some constraints taken from geophysical and geological investigations. Selecting density contrast, mean depth and filtering parameters is essential in the gravity inversion. While the parameters could be determined by the gravimetric method itself or under some assumptions, the best method is to refer to other geophysical exploration. We refer to the density contrast according to a modified model of Haines *et al*. (2003) and carry out spectral analyses on BA, topography and preliminary Moho models to determine filtering parameters and to estimate the mean depth of Moho, determine the effective elastic thickness of lithosphere and the buried loads. Based on the results of the preliminary analysis, gravity inversion is performed to obtain an improved Moho image.

5.1 Spectral analysis

Power spectrum analysis on BA under the white-spectrum assumption has been a useful gravimetric method for depth estimation. Since we focus on the plateau, the spectral analysis is applied to AREA3 (see Fig. 8B for the area). We apply the method of Spector and Grant (1970) that allows to determine the depth of causative bodies by the piecewise linear relation between the logarithm of the squared spectral amplitude and the wavenumber. We find two depths, relative to the reference height of 7 km, which are of 216 and 54 km, of which uncertainty in the least-square fitting were 35 and 24 km, respectively (Fig. 8A). They can be interpreted as follows: 54 km for the mean Moho depth and 216 km for the detached Asian mantle or crustal multiples (Kind *et al*. 2002). Wavenumbers higher than 0.03 km^{-1} are excluded in this analysis, because they seem to have an abnormally broken pattern around 0.03 km^{-1} and these harmonics of the gravity are thought to be dominated by buried loads, which are discussed below. When we extend the right limit of the wavenumber domain to 0.048 km^{-1} instead of 0.03 km^{-1}, the estimated mean depth is from about 70 to 86 km, which is close to the maximum Moho depth of Tibet rather than mean depth. Extending the spectral window further to around 0.062 km^{-1} makes mean depth of about 54 km with uncertainty of 3 km. These abnormal patterns are seemed to be caused by buried loads, which have to be filtered out for Moho estimation of this study.

We also estimate the coherence that has been successfully used in gravity surveys to estimate the isostatic equilibrium since McKenzie and Bowin (1976) and Forsyth (1985). In the analysis different windows have been used, of which windows named AREA1 and AREA2 mostly exclude the NGZ-area. The comparison of the curves shown in Figs 8(B) and (C) for the different windows shows that the results are stable, and that the effect of the NGZ, if present, is irrelevant, as all four windows essentially give the same result. Fig. 8(B) shows that coherences for waves longer than about 900 km approach unity, implying the Airy-type compensation. On the other hand, the loads of waves shorter than 200 km are found to be fully supported by the rigidity of the lithosphere. The loads of intermediate wavelengths are observed to be supported partially by the rigidity of the lithosphere and also by vertical movement. Effective elastic thickness (EET) is estimated to be about 35 km by comparing observed coherences with predicted ones. The f-ratio, the ratio of bottom to top loading, is 0.5–0.6 overall, while 0.9 for wavelength 280 km and 0.4 for 350 km. The observed weak lithosphere of the plateau seems to be related to partial melting (Kind *et al*. 1996; Nelson *et al*. 1996; Vanderhaeghe & Teyssier 2001) and make the buckling of Moho (Jin *et al*. 1994) possible. Our EET is bigger than those by Braitenberg *et al*. (2003) except in Tarim and Qaidam basin, similar with those by Jin *et al*. (1996) and Caporali (2000) and smaller than those of Wang *et al*. (1997). The EET we estimated is also inevitable from debates as McKenzie (2003) indicates the problem of overestimation of the coherence method when the loads with no topographic expression are important due to erosion and sedimentation. The coherence and coherency curves present a kink at wavelengths 70–180 km, which is interpreted here as buried loads that lie in upper crust. According to Watts (2001), buried loads occur in a wide range of geological settings. In compressional settings, they include the overthrusting of large crustal blocks that causes large-scale flexing of the lithosphere. In extensional settings, they include the effects of heating and cooling the lithosphere, which produce subsidence and uplift.

We find the coherency to be negative at all wavelengths, except near the wavelength of 180 km. We test the coherency analysis for different densities of the topography, varying the values from 2670 to 2470 kg m^{-3}. With a reduction of the density, the coherency moves upwards in the positive direction with keeping its pattern, with small variation at wavelengths greater than 400 km (Fig. 8C). The buried loads of the Tibetan plateau were also reported by Jin *et al*. (1994) based on the interpretation of coherence, while their values of observed coherence reached up to about 0.4 between 100 and 200 km. The coherence and coherency of our study shows similar pattern with Jin *et al*. (1994) as a whole, however the details are different especially at short wavelengths.

5.2 Moho undulations

Braitenberg *et al*. (2000a,b, 2003) applied a gravity inverse method to the computation of the Moho structure. It results that the Moho undulations are of sufficient wavelength (200 km and upwards) to be seen by the spherical harmonic expansion of the gravity field up to degree and order 360 that is equivalent to a distinguishable pixel size at the equator of near to 55 km, and even smaller at higher latitudes (e.g. Hofmann-Wellenhof & Moritz 2005). Their models however cover a smaller area of the Tibet plateau than our study, due to limitations in data coverage. This limitation is now lifted by the GRACE mission, which has provided a precise gravity data set uniformly covering the whole of the plateau and its neighbouring areas. Moreover, according to the resolution of GRACE gravity and Power Spectral Densities (PSDs) of BA and preliminary Moho models (Fig. 9), the satellite-only data turns out to have resolution that is high enough to recover signals generated by the very deep Moho beneath Tibet.

The resolution of the Moho models can be estimated by inverting the GRACE error curve to a given depth-level, obtaining the minimum observable oscillation amplitude of the Moho sorted by the oscillation wavenumber, or, equivalently the degree of the harmonic expansion. A first-order inversion is accomplished by the downward continuation to different depths, and assuming a standard value for the density contrast at the Moho (here we used 500 kg m^{-3}). We used the depths at 10 km intervals between 30 and 70 km, the results being shown in Fig. 10. The minimum resolvable oscillation

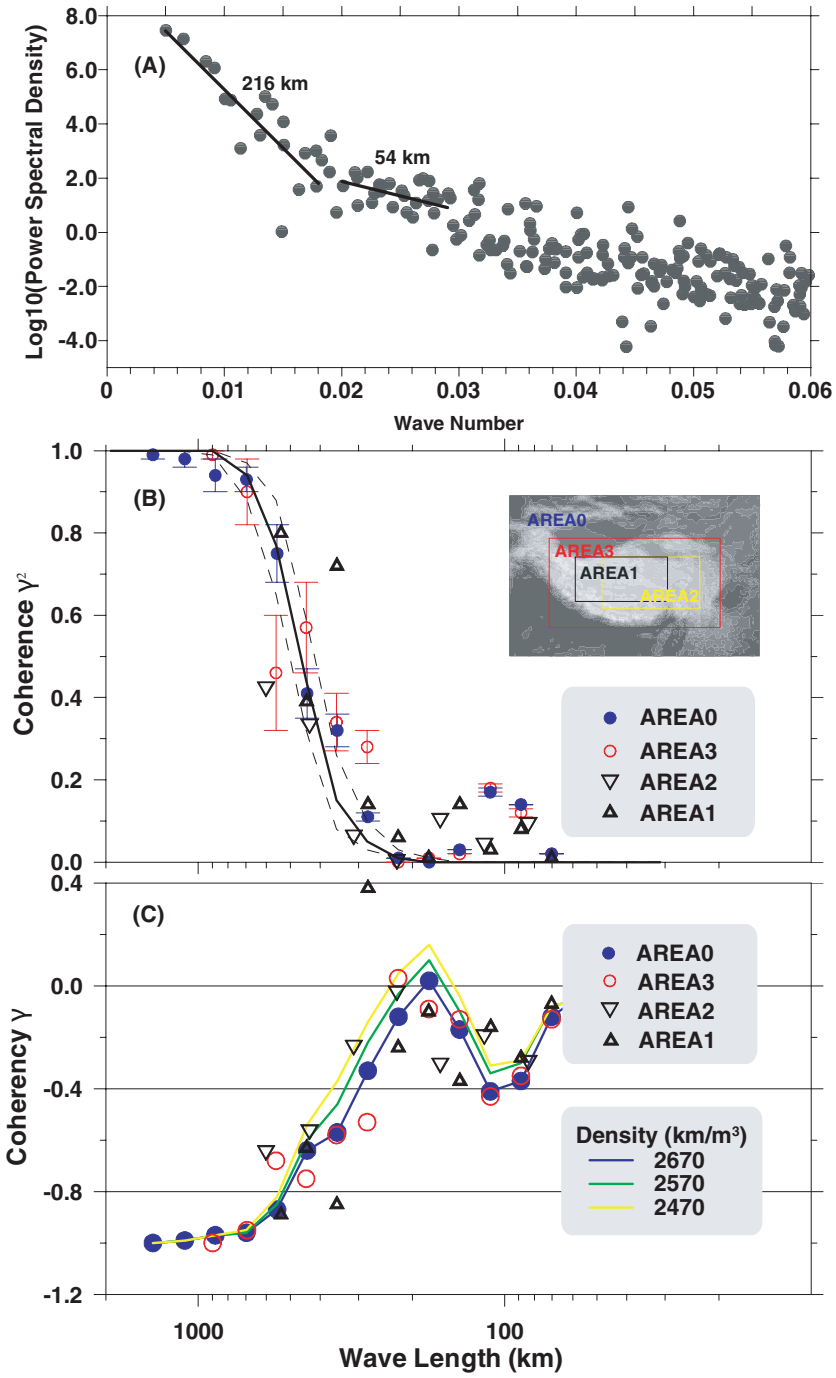

Figure 8. Spectral analyses: (A) Power spectral analysis for mean depth estimation. Bouguer anomaly (BA) of AREA3 is used. The estimated depths are referred to the reference level of 7 km height. (B) Coherence between BA and topography. Buried loads are observed at wavelengths between 70 and 180 km. Predicted coherences are presented in one solid and two dashed lines, which correspond to effective elastic thickness of 35, 40 and 30 km, respectively. (C) Coherency between BA and topography. It is shown that the buried load has negative coherency except in small range of wavelength around 180 km. As the density becomes low the coherency moves in the positive direction with keeping its pattern, though it changes little in the range of waves shorter than 80 km and longer than 400 km.

amplitude is inversely proportional to the density contrast at the Moho. It can be seen that the resolution at degree 200 is near to 2 km, sufficient to detect Moho undulations set at about 70 km. The resolution is even better for the density contrast we find further down to be more appropriate for the Tibet plateau (368 kg m^{-3}).

In order to separate the gravity signals generated from the Moho and from buried crustal density-inhomogeneities from the total BA signal, we integrate the isostatic analysis with the spectral analysis shown above. The problem consists in defining the appropriate limits of the frequency filtering that separates the contributions from the sources set at different depths. The coherence and coherency analysis showed that the buried loads, which correspond to the crustal density inhomogeneities, pertain to wavelengths shorter than about 220 km (see green line of Fig. 8C). This wavelength, therefore, will

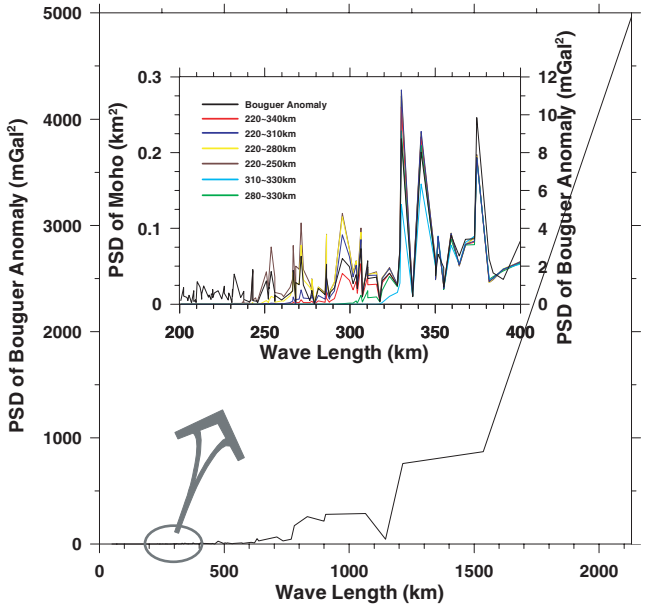

Figure 9. Power spectral analysis of Bouguer anomaly and several cases of preliminary Moho models: Black solid line represents Bouguer anomaly and the other lines denote preliminary Moho models. The km-bands correspond to filtering parameters, w_1 and w_2 of eq. (7), respectively.

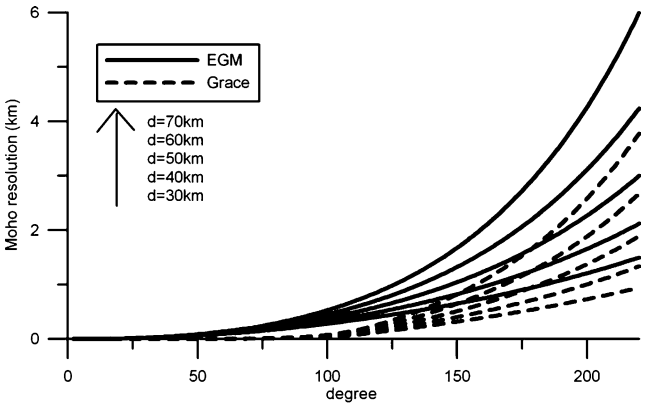

Figure 10. Resolution power of the GRACE gravity field in the estimate of Moho undulations. Set of curves pertain to average Moho-depths between 30 and 70 km. The curves were obtained by inverting the accumulated error curve for GRACE and EGM96 (Fig. 2). Density at Moho: 500 kg m^{-3}. The resolution is even better for smaller densities.

constitute the upper frequency limit used in the Moho inversion. The overall pattern of the energy spectrum of the BA (Fig. 9) shows that a substantial part of the spectral energy is distributed at very long wavelengths between 600 and 1100 km. In the greater Tibet area this energy can be attributed to the isostatic response to topography, considering high coherence (Fig. 8B) and the size of the entire Tibet plateau and of the Tarim basin. Observing the shorter wavelengths carefully (see inlay in Fig. 9, with enlarged portion of the spectrum), three spectral peaks are evident, at wavelengths of 330, 340 and 375 km (corresponds to wavenumbers $k = 0.019$, 0.0185 and 0.0168 km^{-1}, respectively): we interpret them as signals of the Moho undulation due to compressional deformation.

Going back to the analysis of the depth sources corresponding to different frequency ranges (Fig. 8A), we conclude that these frequencies are due to the Moho, as they are found at wavenumbers

Table 1. Gravity inversion statistics in Moho computation.

	Mean	*SD*	Minimum	Maximum
(1) Input BA	−230.8	155.8	−561.5	26.1
(2) Output Moho Depth	−47.0	12.0	−79.5	−27.9
(3) Gravity caused by (2)	−230.8	155.8	−558.9	24.6
(4) Difference of (3) and (1)	0.00	0.91	−4.85	5.99

Notes. Gravity anomalies in (1), (3) and (4) are in MGal unit, and Moho depth in km. Computation is performed on an area (x: −1900 to 1910 km, y: −1260 to 1280 km) slightly wider than study area (x: −1700 to 1700 km, y: −1100 to 1100 km) and mirroring technique is applied to treat the Gibbs phenomenon. Filter is designed with $w_1 = 0.02026$, $w_2 = 0.02828$ and $kp = 1$; convergence criteria are set to rms = 1.0e−3 and Sn/S2 = 1.0e−4; normal crust thickness 32.0 km; density contrast 368 kg m^{-3}. After 10th iteration, the convergence criteria are satisfied, while the expected rms of residual Moho undulations is estimated to be 0.7 m.

between the two trends we have found. From the spectral analysis it could be argued that the longest wavelengths should be eliminated as well. This though has not given satisfying results, due to the fact that the wavenumbers to be eliminated are mainly originated by regional isostatic Moho and compressional deformation. As mentioned in the introduction the greatest density jump in the lithosphere occurs at the Moho and the other deeper contrast is much less effective. Therefore, we come to the conclusion, that it is preferable to maintain the lowest wavenumbers.

We therefore, conclude that wavelengths smaller than 220 km must be eliminated and wavelengths longer than 330 km maintained in the BA spectrum prior inversion. The question remains how to choose the two corner frequencies of the filter function (eq. 7). In Fig. 9, we show the effects of the choice of different corner-frequencies of the low-pass filter (expressed in terms of wavelengths). The choice of the wavelengths 220 and 310 km seems the best choice, as the Moho reflects well the above spectral peaks. Also the other proposed windows are acceptable, except the choice with corner wavelengths 310–330 km, with which the wavelengths near 330 km are visibly damped. We therefore, designed a low-pass filter with the properties that waves longer than 310 km pass through the filter thoroughly, but waves shorter than 220 km are cut-off, while intermediate waves pass partly (see footnote of Table 1 for details on filtering and convergence parameters, and also Fig. 7 for the low-pass filtered BA). We also examined the influence of the filter parameter on the Moho result. In the following we give the difference of the respective Moho solution with our preferred Moho solution obtained with filter decay function between wavelengths 220 and 310 km. We calculated *SD* and maximum and minimum difference of the two solutions obtaining (1) (*SD* 0.67, minimum −0.92 and maximum 3.61 km) for filter parameter 220–250 km, (2) (*SD* 0.29, minimum −1.55 and maximum 1.47) for 220–280 km, (3) (*SD* 0.22, minimum −1.18 and maximum 1.17) for 220–340 km, (4) (*SD* 0.78, minimum −3.95 and maximum 3.98) for 280–330 km, (5) (*SD* 1.06, minimum −5.45 and minimum 5.28) for 310–330 km, and averages of the differences being 0.0 km. We thus find that the shapes of the Moho solutions are very similar to each other, even in the case of the filter parameter 310–330 km. Considering the above analyses, we can conclude that even the satellite-only model of GRACE has most of the signals needed for the Moho estimation, especially the prevailing wavelengths, which we interpret further down as being due to the collisional compression.

The other parameters that determine the outcome of the inversion are the reference crustal thickness, the density of sediments and the density contrast at the Moho. We refer to the seismic section INDEPTH III (Haines *et al*. 2003), to define these parameters.

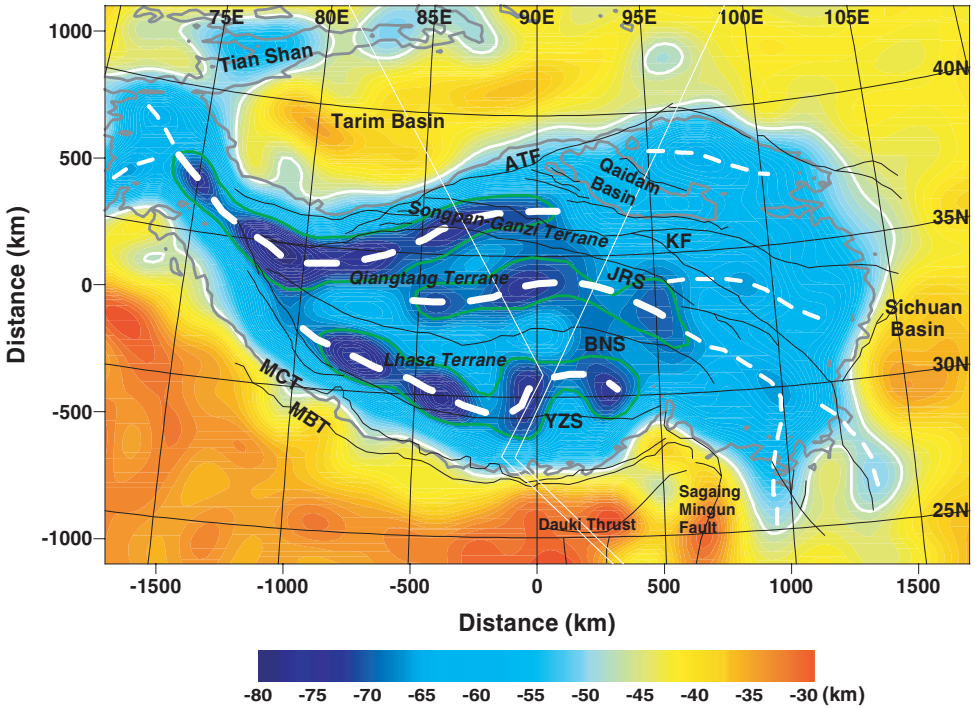

Figure 11. Moho image beneath Tibet: Normal crust thickness is estimated to be 32.0 km and *SD* of Moho undulation 12.0 km, when mean depth is set to 47.0 km (below MSL) and density contrast 368 kg m^{-3}. Three deep Moho belts (green solid line) are shown clearly with E–W trends, and raised belts between them, especially along BNS. The deepest Moho up to 79.5 km is found in western Tibet. Moho undulations are in good agreement with the main tectonic sutures. Tectonic lines are labelled with acronyms as MBT (Main Himalaya Thrust), MCT (Main Central Thrust), YZS (Yarlung-Zangbo Suture), BNS (Bangong-Nujiang Suture), JRS (Jinsha River Suture), KF (Kunlun Fault) and ATF (Altyn Tagh Fault). Grey line bordering the plateau represents 3-km-height level. Thick white line denotes 47-km depth of Moho, of which distribution is similar to the 2-km-height topography line (not shown here). White dashed lines are used to describe 'Moho ranges' (thicker dashed lines are used for the large scale troughs). Profiles along two white lines are given in Fig. 13.

Referring to the INDEPTH III section we assume the density of topography above MSL to be 2570 kg m^{-3} and the sediment density to be 2465 kg m^{-3}, while the density contrast at the Moho discontinuity is set to be 368 kg m^{-3} and the density contrast of the buried load is set to be 291 kg m^{-3}. The lower density of the topography with respect to the standard value 2670 kg m^{-3} makes the recalculation of the BA necessary and affects also the sediment correction. We have preferred to keep the previous discussion with standard values, in order to make it more comparable with studies made in other areas. The main features obtained above for the spectral and isostatic analysis are not affected by the density change. We estimate the reference depth using the above value for mean Moho depth ($d_{\mathrm{mean}} = 47$ km $= 54 - 7$ km), the average gravity anomaly ($dg_{\mathrm{mean}} = -231$ MGal) and the density contrast ($\rho_1 = 368$ kg m^{-3}) through the relation $d_{\mathrm{ref}} = d_{\mathrm{mean}} - dg_{\mathrm{mean}}/2\pi G\rho_1 = 32$ km, which indicates that Tibet has a typical reference depth of continental crust from an isostatic view, even though the crustal thickness is double that of other ordinary continents. The reference depth and density are compatible with the values used in the previous gravity inversion of Braitenberg *et al*. (2000a,b), based on a best approximation to the constraining seismic lines.

Fig. 11 shows the Moho undulations of Tibet, using the above parameters and the Parker–Oldenburg inversion method (Parker 1972; Oldenburg 1974; Shin *et al*. 2006); the smooth convergence of the iterations is seen in Fig. 12, where the residual rms difference of the Moho between successive iterations is graphed for the increasing iteration-steps. The final rms correction of the Moho at the 10th iteration with respect to the previous iteration is of only 0.7 m. The inversion was performed on an area (x: −1900 to 1910 km, y: −1260 to 1280 km) slightly wider than the study area (x: −1700 to 1700 km, y: −1100 to 1100 km) and focused on the plateau. A mirroring technique was applied to treat the Gibbs phenomenon. The gravity effect of the computed Moho model showed only small discrepancies from the input gravity data within −4.85 to 5.99 MGal with average 0.00 MGal and *SD* 0.91 MGal (Table 1).

The Moho is observed generally to be deeper than about 47 km, while the maximum depth, 79.5 km is found in west Tibet and the minimum depth, 27.9 km near the Dauki Thrust, which is beyond the study area. The Moho is found to be very deep in western and central Tibet, while a relatively shallow Moho, with values less than 65 km is widely found in eastern Tibet. For the Tibetan Plateau we obtain three deep E–W trending Moho belts, that starting from south to north are in the southern part of the Lhasa terrain, in the Qiangtang terrain, and in the Songpan-Ganzi terrain. The northern-most deep belt changes direction at approximately 80°E (Ladakh), continuing northwest-wards, following the Karakoram range. The three deep belts are separated by shallower Moho belts. The Tarim basin is underlain by Moho values between 35 and 47 km. The Bachu uplift in the Tarim basin (e.g. Sobel *et al*. 2003), is accompanied by a shallowing of the Moho. The Tien Shan range to the north of the Tarim basin has deeper Moho depth values.

We have tested the effect of the density variation, by considering two values above (468 kg m^{-3}) and below (268 kg m^{-3}) our preferred value. For the upper value, the Moho varies between 31.9 and 71.8 km with *SD* of the undulation 9.4 km and reference depth of 35.0 km. When the density contrast 268 kg m^{-3}, the Moho varies between 21.3 and 94.2 km with *SD* 16.5 km and the reference depth results to be 26.5 km, which can be hardly acceptable for the

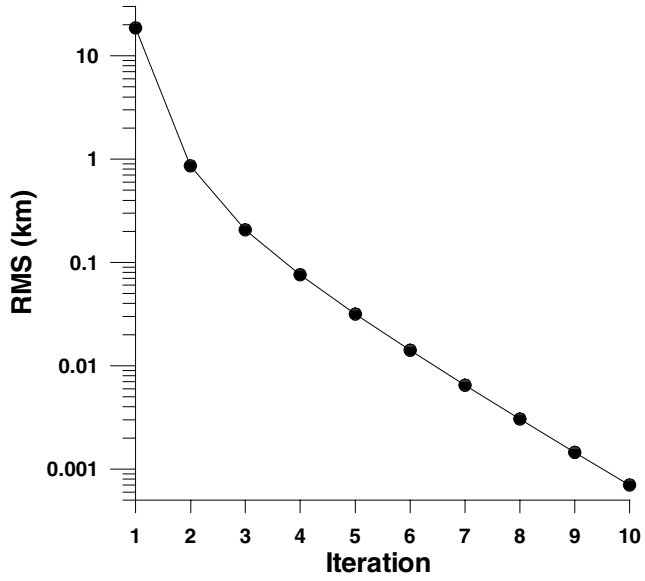

Figure 12. Convergence rate of gravity inversion: rms denotes difference of Moho between successive iterations.

continental crust. The Moho solutions for the different density values are seen in Fig. 13, where the inverted Moho is plotted along two profiles crossing the plateau (east and west line, Figs 1 and 11), together with the seismic Moho. It can be seen how the reduction of the density is reflected in an increase of the oscillation amplitude of the Moho. Local isostatic Moho models according to the Airy/Heiskanen hypothesis are also computed and compared: to find isostatic Moho models that fit well with the gravity inversion model, the density of topography is assumed as 2570 kg m^{-3} like above and density contrast at Moho and reference depth are varied with intervals of 5 kg m^{-3} and 0.01 km, respectively. As a result a minimum rms difference between the two models is 3.5 km when the density contrast is 390 kg m^{-3} and the reference depth is 33.38 km, which are very similar to the assumed values for gravity inversion. The Airy/Haiskanen Moho is also shown along two profiles in Fig. 13.

The Moho is seen in Fig. 13 to be deep on a large scale along southern Tibet below the YZS, and it reduces its depth beneath the BNS. The Moho shows greater oscillation along the west line, whereas it gently reduces its depth northwards along the east line. The seismic results show an overall similar pattern compared with our gravity inversion model, although the seismic Moho is deeper beneath YZS by as much as 10–20 km. It should be noticed that there are considerable differences between different seismic experiments and also that the location of the seismic stations are not exactly coincident with the cross-sectional lines (Fig. 1). This could also be the cause of some of the discrepancies found.

6 DISCUSSION

We have used the recent satellite derived gravity field to determine the Moho undulations in the Tibet-Quinghai plateau and surrounding areas. Our approach inverts the Bouguer gravity anomalies corrected for the contributions due to the sediments. Presently it is not advisable to correct for the inhomogeneities below the Moho, as due to lithospheric thickening, or lithospheric subduction, as there are great uncertainties in the extent of the lithospheric subduction, and the exact form of lithospheric thickening. Previous works (Jin *et al*. 1996; Braitenberg *et al*. 2000) have estimated the gravity effect of lithospheric thickening and have shown that over the Tibet plateau the gravity effect is near to constant, with variation of near to 10 MGal. We conclude that neglecting the lithsophere thickening, will not contribute to the Moho undulations we observe, but at the most contribute to a constant depth value. We assume a constant density contrast at the Moho level, also due to the fact that the constraints are insufficient to safely introduce reliable density variations. The density contrast acts as a linear scaling parameter to the Moho undulations. A certain increase in the density contrast, therefore, would correspond in a proportional reduction in the inverted Moho amplitudes. From a purely theoretical point of view, the undulating signal present in the gravity field could be interpreted as being due to lateral density variations in the crust. Assuming a lower crustal layer of 20 km thickness, the density variations would be in the order of 0.15 kg m^{-3}. This value is rather high to be realistic. Moreover, the seismologic and seismic investigations converge to a variation of Moho depth across Tibet, which is in accord with the depth variation we have inferred from our model.

We obtain a Moho that presents three deep belts (troughs) with shallower belts (ridges) between them, with a clear E–W oriented trend parallel to the plateau border and suture lines, while a variation of the trends is observed in central to southeast Tibet. One of the thin belts along BNS is remarkable, the depth of which is less than 65 km (down to 62 km). To describe the distinctive shape of the Moho troughs beneath Tibet, we introduce the term 'Moho ranges', for it resembles a mountain range not only in shape (in negative direction) but also in origin. The term 'Moho ranges' can inspire a different extent of understanding of the characteristics of Moho undulation, compared to the well known and widely used terms like Moho undulation, ridges and troughs: the former emphasizes the fact that the origin of the structure is closely related with the compressional forces due to collision and results in mountain range-like structure, while the latter terms have been used mainly to describe the shapes that were formed by vertical deflection in response to isostasy or due to other causes. The most interesting patterns of the Moho ranges are 1) that they run in parallel with the border and the principal sutures of the plateau, (2) that the distances between ranges are in regular values of about 330 km except in northeast Tibet and (3) that the splitting of the ranges into two branches is found as the distance between the ranges is increasing. Our result is, therefore, consistent with an interpretation of having the superposition of two effects: first, the isostatic response to the topographic load, which produces a crustal thicknening and second a buckling of the lithosphere due to the compressive plate-stresses.

One point of criticism could be set forward, based on the fact that the wavelength of the Moho ranges (spectral peaks found at wavelengths between 330 and 375 km) is close to the shortest wavelength of the satellite-only GRACE spherical development, which is up to degree and order 120. The wavelength of 350 km in fact corresponds to a spherical harmonic degree of about 114. The sceptical reader could thus ascribe the observed depth variations to noise in the satellite derived gravity data. To this objection, the following can be said: (1) the previous study, based on terrestrial-only data, with a mean grid-spacing of 25 km, which is a much higher spatial resolution than the 360 spherical development, found the same E–W trending undulations in the gravity field and consequently in the Moho inversion, (2) the undulations correlate well with the major suture lines, which is highly improbable in the case the signals were pure noise and (3) the undulations are consistent with the depth variations found from seismic investigations.

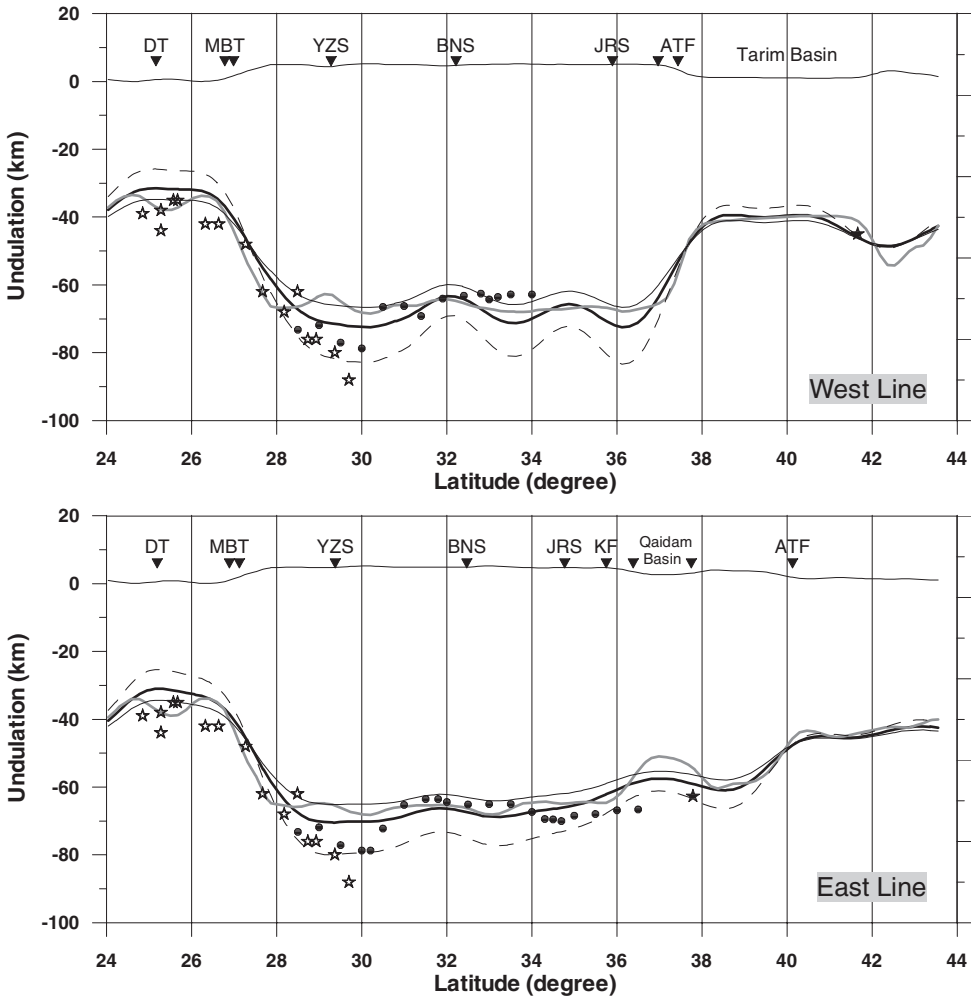

Figure 13. Profiles along west and east lines (see Figs 1 and 10): Thick line, dashed and thin line represent gravimetric Moho models of density contrast 368, 268 and 468 kg m^{-3}, respectively. The upper-thin and grey-thick lines denote topography and isostatic Moho that fit well with gravimetric Moho model, respectively. The inverse triangles represent cross-over points with tectonic lines shown with acronyms like DT (Dauki Thrust), MBT (Main Himalaya Thrust), YZS (Yarlung-Zangbo Suture), BNS (Bangong-Nujiang Suture), JRS (Jinsha River Suture), KF (Kunlun Fault) and ATF (Altyn Tagh Fault). Solid circles, open and solid stars are Moho depths from Kind *et al*. (2002), Mitra *et al*. (2005) and Zhao *et al*. (2006), respectively.

7 CONCLUSIONS

Our Moho model is the first one that can cover the whole of the Tibetan plateau and Tarim and Qaidam basins by using the most advanced satellite gravity of GRACE in estimating the Moho undulation. According to our analysis, the GRACE satellite-only data turns out to have resolution that is high enough to recover signals for the very deep Moho beneath Tibet. We suggest that one should set a reference level just above the topography of the study area for gravity anomaly computation, if one uses satellite-based gravity models like the GGM series, EGM96, etc., which have no height information of observation stations. We also suggest a NGZ correction that is very useful in the area where no surface gravity data is available in EGM96, since we now have higher resolution satellite gravity data of GRACE. However the satellite-only gravity data up to now still does not have high enough spatial resolution for estimating the normal Moho undulations that lie about 30 km below MSL, while the abnormally very deep Moho beneath Tibet, that has long wavelength variations, could be thought as an exceptional case as shown in our analysis.

Our Moho model of the Tibetan plateau reveals the feature of Moho ranges and is characterized by the three deep Moho belts (troughs) and shallow belts (ridges) between them, which have not been clearly distinguished before. The existence of a deep Moho along the southern and northern border of the plateau and of a shallow Moho beneath the BNS finds confirmation in seismic (King *et al*. 2002) and previous gravimetric investigations (Braitenberg *et al*. 2000a,b, 2003). Our result shows that the Moho deepening and northward shallowing found north of the YZS (Kind *et al*. 2002; Mitra *et al*. 2005) can be extended westwards along the Lhasa terrain for about 800 km, and eastwards to about 200 km. Our study also emphasizes that the distinctive undulation features of the Moho could have been formed by buckling in compressional environment, while the greatly deep Moho is mainly due to isostatic compensation of topography.

Therefore, this study may give some new constraints on the dynamic modelling of the buckled structure of the Tibet area. We hope our new Moho model will give new insights regarding the geohistory, buckling mechanism and crustal movements beneath Tibet.

ACKNOWLEDGMENT

We express many thanks to unknown reviewers, and to Dr Lee, Dr McNutt and Mr Steven for their advice. This work was supported by the Post-doctoral Fellowship Program of Korea Science & Engineering Foundation (KOSEF) and improved by the support of Korea Astronomy and Space Science Institute. We also appreciate the care and support of IGG, CAS. We acknowledge a CAS-CNR exchange program between the Trieste University and the IGG, CAS.

REFERENCES

Blakely, R. J., 1995. *Potential Theory in Gravity and Magnetic Applications*, Cambridge University Press, New York, USA.

Braitenberg, C., Zadro, M., Fang, J., Wang, Y. & Hsu, H.T., 2000a. Gravity Inversion in Qinghai-Tibet Plateau, *Phys. Chem. Earth (A),* **25,** 381–386.

Braitenberg, C., Zadro, M., Fang, J., Wang, Y. & Hsu, H.T., 2000b. The gravity and isostatic Moho undulations in Qinghai-Tibet Plateau, *J. Geodyn.,* **30,** 489–505.

Braitenberg, C., Wang, Y., Fang, J. & Hsu, H.T., 2003. Spatial variations of flexure parameters over the Tibet-Qinghai Plateau, *Earth Planet. Sci. Lett.,* **205,** 211–224.

Caporali, A., 2000. Buckling of the lithosphere in western Himalaya: Constraints from gravity and topography data, *J. Geophys. Res.,* **105,** 3103–3113.

Chen, Z.Q. & Shi, G.R., 2003. Late Paleozoic depositional history of the Tarim basin, northwest China: an integration of biostratigraphic and lithostratigraphic constraints, *AAPG Bull.,* **87,** 1323–1354.

Cruz, J. Y. & Laskowski, P., 1984. *Upward Continuation of Surface Gravity Anomalies*. Department of Geodetic Science and Surveying, Ohio State University, Report No. 360.

Förste, C. *et al.*, 2006. A mean global gravity field model from the combination of satellite mission and altimetry/gravimetry surface data – EIGEN-GL04C, *Geophys. Res. Abstracts*, **8**, 03462.

Forsyth, D.W., 1985. Subsurface loading and estimates of the flexural rigidity of continental lithosphere, *J. Geophys. Res.,* **90,** 12 623–12 632.

Haines, S.S., Klemperer, S.L., Brown, L., Jingru, G., Mechie, J., Meissner, R., Ross, A. & Wenjin, Z., 2003. INDEPTH III seismic data: From surface observations to deep crustal processes in Tibet, *Tectonics,* **22**(1), 1001, doi:10.1029/2001TC001305.

Heiskanen, W.A. & Moritz, H., 1987. *Physical Geodesy*, Institute of Physical Geodesy, Technical University, Graz, Austria.

Hofmann-Wellenhof, B. & Moritz, H., 2005. *Physical Geodesy*, Springer Verlag, Wien, pp. 1–403.

Jiang, X. & Jin, Y., 2005. Mapping the deep lithospheric structure beneath the eastern margin of the Tibetan Plateau from gravity anomalies, *J. Geophys. Res.,* **110,** B07407, doi:10.1029/2004JB003394, 1–14.

Jin, Y., McNutt, M.K. & Zhu, Y-S., 1994. Evidence from gravity and topography data for folding of Tibet, *Science,* **371,** 669–674.

Jin, Y., McNutt, M.K. & Zhu, Y-S., 1996. Mapping the descent of Indian and Eurasian plates beneath the Tibetan Plateau from gravity anomalies, *J. Geophys. Res.,* **101,** 11275–11290.

Kind, R. *et al.*, 1996. Evidence from earthquake data for a partially molten crustal layer in southern Tibet, *Science,* **274,** 1692–1694.

Kind, R. *et al.*, 2002. seismic images of crust and upper mantle beneath Tibet: evidence for Eurasian Plate subduction, *Science,* **298,** 1219–1221.

Lemoine, F.G. *et al.*, 1998. The Development of the Joint NASA GSFC and the Mational Imagery and mapping Agency (NIMA) Geopotential Model EGM96, NASA/TP-1998-206861.

Lithospheric Dynamic Atlas of China, 1989. China Cartographic Publishing House, Beijing.

Lyon-Caen, H. & Molnar, P., 1983. Constraints on the structure of the Himalaya from an analysis of gravity anomalies and a flexural model of the lithosphere, *J. Geophys. Res.,* **88,** 8171–8191.

McKenzie, D., 2003. Estimating Te in the presence of internal loads, *J. Geophys. Res.,* **108,** doi:10.1029/2002JB001766.

Mckenzie, D.P. & Bowin, C.O., 1976. The relationship between bathymetry and gravity in the Atlantic Ocean, *J. Geophys. Res.,* **81,** 1903–1915.

Mitra, S., Priestley, K., Bhattacharyya, A. & Gaur, V.K., 2005. Crutsal structure and earthquake focal depths beneath northeastern India and southern Tibet, *Geophys. J. Int.,* **160,** 227–248.

Nelson, K.D. *et al.*, 1996. Partially molten middle crust beneath southern Tibet: Synthesis of project INDEPTH results, *Science,* **274,** 1684–1688.

Oldenburg, D.W., 1974. The inversion and interpretation of gravity anomalies, *Geophysics,* **39,** 526–536.

Parker, R. L., 1972. The rapid calculation of potential anomalies, *Geophys. J. R. Astr. Soc.,* **31,** 447–455.

Qiusheng, L. *et al.*, 2002. Tarim underthrust beneath western Kunlun; evidence from wide-angle seismic sounding, in *15th international Himalaya-Karakoram-Tibet Workshop*, eds. Wang, C., Wilson, C.J.L. & Searle M.P., *J. Asian Earth Sci.,* **20,** 247–253.

Shin, Y.H., Choi, K.S. & Xu, H., 2006. Three-dimensional forward and inverse models for gravity fields based on the fast Fourier Transform, *Com. Geosci.,* **32,** 727–738.

Sobel, E.R., Hilley, G.E. & Strecker, M.R., 2003, Formation of internally drained contractional basins by aridity-limited bedrock incision, *J. Geophys. Res.,* **108** (B7), 2344, doi:10.1029/2002JB001883.

Spector, A. & Grant, F.S., 1970. Statistical models for interpreting aeromagnetic data, *Geophysics.*, **35,** 293–302.

Tapley, B. *et al.*, 2005. GGM02 – An improved Earth gravity field model from GRACE, *J. Geodesy.*, doi:10.1007/s00190–005-0480-z.

Vanderhaeghe, O. & Teyssier, C., 2001. Partial melting and flow of orogens, *Tectonophyscs,* **342,** 451–472.

Wang, Y., Feng, R. & Hsu, H., 1997. Lithospheric isostasy, flexure and the strength of upper mantle in Tibetan plateau, *Proc. 30th Int'l Geol. Congr.,* **4,** 153–160.

Watts, A.B., 2001. *Isostasy and Flexure of the Lithosphere*, Cambridge University Press, Cambridge, UK.

Zhao, J., Mooney, W.D., Xiankang, Z., Zhichun, L., Zhijun, J. & Okaya, N., 2006. Crustal structure across the Altyn Tagh Range at the northern margin of the Tibetan plateau and tectonic implications, *Earth Planet. Sci. Lett.,* **241**(3–4), 804–814.

Zhou, R., Grand, S.P., Tajima, F. & Ding, X.-Y., 1998. High velocity zone beneath southern Tibetan Plateau and implications for the regional mantle dynamics, in *Mantle Dynamics and Plate Interactions in East Asia*, pp. 25–45, Vol. 27, eds. M.F.J. Flower, S.L. Chung, C.H. Lo & T.Y. Lee, Geodynamics Series, AGU, Washington, DC.